Herschel observations of Cen A

Auld, R.; Smith, M. W. L.; Bendo, G.; Pohlen, M.; Wilson, C.; Gomez, H.; Cortese, L.; Morganti, R.; Baes, M.; Boselli, A.

Published in:
Monthly Notices of the Royal Astronomical Society

DOI:
10.1111/j.1365-2966.2011.19819.x

Publication date:
2012

Monthly Notices
of the
ROYAL ASTRONOMICAL SOCIETY

Mon. Not. R. Astron. Soc. **420,** 1882–1896 (2012) doi:10.1111/j.1365-2966.2011.19819.x

Herschel observations of Cen A: stellar heating of two extragalactic dust clouds

R. Auld,[1⋆] M. W. L. Smith,[1] G. Bendo,[2] M. Pohlen,[1] C. Wilson,[3] H. Gomez,[1] L. Cortese,[4] R. Morganti,[5,6] M. Baes,[7] A. Boselli,[8] A. Cooray,[9,10] J. I. Davies,[1] S. Eales,[1] D. Elbaz,[11] M. Galametz,[12] K. Isaak,[13] T. Oosterloo,[5,6] M. Page,[14] E. Rigby,[15] L. Spinoglio[16] and C. Struve[5,6]

[1]*School of Physics and Astronomy, Cardiff University, Queens Buildings, The Parade, Cardiff CF24 3AA*
[2]*Jodrell Bank Centre for Astrophysics, School of Physics and Astronomy University of Manchester, Oxford Road, Manchester M13 9PL*
[3]*Department of Physics & Astronomy, McMaster University, Hamilton, Ontario L8S 4M1, Canada*
[4]*European Southern Observatory, Karl-Schwarzschild Str. 2, 85748 Garching bei Muenchen, Germany*
[5]*Netherlands Institute for Radio Astronomy, Postbus 2, 7990 AA Dwingeloo, the Netherlands*
[6]*Kapteyn Astronomical Institute, University of Groningen, PO Box 800, 9700 AV Groningen, the Netherlands*
[7]*Sterrenkundig Observatorium, Universiteit Gent, B-9000 Gent, Belgium*
[8]*Laboratoire d'Astrophysique de Marseille, 13388 Marseille, France*
[9]*Department of Physics & Astronomy, University of California, Irvine, CA 92697, USA*
[10]*California Institute of Technology, 1200 E. California Blvd, Pasadena, CA 91125, USA*
[11]*Laboratoire AIM-Paris-Saclay, CEA/DSM/Irfu – CNRS – Université Paris Diderot, CE-Saclay, pt courrier 131, F-91191 Gif-sur-Yvette, France*
[12]*Institute of Astronomy, University of Cambridge, Madingley Road, Cambridge CB3 0HA*
[13]*European Space & Technology Centre (ESTEC), PO Box 299, 2200 AG Noordwijk, the Netherlands*
[14]*UCL, Mullard Space Science Laboratory, Holmbury St Mary, Dorking, Surrey RH5 6NT*
[15]*School of Physics and Astronomy, University of Nottingham, University Park, Nottingham NG7 2RD*
[16]*IFSI Roma, Via del Fosso del Cavaliere, 100 00133 Roma, Italy*

Accepted 2011 September 11. Received 2011 August 24; in original form 2011 May 11

ABSTRACT

We present the first results of a multiwavelength survey, incorporating *Herschel*-SPIRE, *Spitzer*, *GALEX* and Australian Telescope Compact Array (ATCA) observations, of a $1^\circ \times 1^\circ$ field centred on Centaurus A. As well as detecting the inner lobes of the active galactic nucleus (AGN) jet and counterjet, we have found two clouds, bright at submillimetre wavelengths, ∼15 kpc from the centre of Cen A that are co-aligned with the jets. Flux measurements at *Herschel* wavelengths have proved vital in constraining fits to the spectral energy distributions (SEDs). The clouds are well fitted by a single-temperature, modified blackbody spectrum ($\beta = 2$) indicating that we are looking at two cold dust clouds on the outskirts of Cen A. The temperature and masses of the clouds are $T_{\rm north} = 12.6^{+1.1}_{-1.2}$ K, $T_{\rm south} = 15.1^{+1.7}_{-1.6}$ K; $\log(M_{\rm north}/{\rm M}_\odot) = 5.8^{+0.2}_{-0.2}$, $\log(M_{\rm south}/{\rm M}_\odot) = 5.6^{+0.2}_{-0.2}$ and the gas-dust ratio for both clouds is ∼100. The measured values for the northern dust cloud are consistent with previous measurements from *ISO* while the southern cloud is a new submillimetre detection. The two dust clouds are located at the termini of the partial H I ring that surrounds Cen A which is also where the gas column density peaks. The *Herschel* survey encompasses the partial H I ring yet we find no evidence of dust emission in any other part of the ring. Assuming that the gas–dust ratio is the same in the rest of the ring, dust mass upper limits in the H I ring are consistent with low column density dust being present but falling below the SPIRE detection limit. We have discussed the origin of these clouds and various possible heating mechanisms. The observations favour a scenario in which the gas and dust were once part of a late-type galaxy, which

⋆E-mail: robbie.auld@astro.cf.ac.uk

has since merged with Cen A. The dominant heating mechanism which adequately explains the observed temperatures in both clouds is heating from the evolved stellar population within Cen A.

Key words: dust, extinction – galaxies: active – galaxies: ISM – galaxies: jets – submillimetre: galaxies – submillimetre: ISM.

1 INTRODUCTION

1.1 Cen A and its environment

Centaurus A (NGC 5128) is the dominant, elliptical galaxy at the heart of the Centaurus group, 3.6 Mpc away (Chattopadhyay et al. 2009). It exhibits a complex variety of gas, dust and stellar structures, observable throughout the electromagnetic spectrum, on scales ranging from sub-pc to kpc scales.

Optical broad-band images are dominated by an aging stellar population (Soria et al. 1996), arranged in a system of shells (Peng et al. 2002), extending out to ∼15 kpc. Bisecting the galaxy along its minor axis is a prominent dust lane, first observed by John Herschel (1847). The optical shells and the presence of a large amount of dust are unusual properties for an elliptical galaxy and are indicative of a past merger with a late-type galaxy, rich in dust and gas (Baade & Minkowski 1954; Malin, Quinn & Graham 1983).

Optical spectroscopy of the interstellar medium (ISM) has revealed star-forming regions and filaments of highly excited gas (Blanco et al. 1975; Peterson, Dickens & Cannon 1975; Morganti et al. 1991, 1992; Rejkuba et al. 2002). The high-ionization states have been interpreted as due to either a beamed ionizing source emanating from the nucleus (Morganti et al. 1991) or shocks being driven into the ISM (Bicknell 1991; Sutherland, Bicknell & Dopita 1993; Fragile et al. 2004).

At radio wavelengths, spectral line observations have detected atomic, molecular and ionized gas in the dusty disc, while wide-field observations in the near vicinity of Cen A have revealed gas in a huge broken ring surrounding the galaxy at a projected distance of ∼15 kpc. The ring contains substantial amounts of atomic (Schiminovich et al. 1994; Oosterloo & Morganti 2005; Struve et al. 2010) and molecular gas (Charmandaris, Combes & van der Hulst 2000) and the velocity structure varies smoothly over the extent of the ring, consistent with rotation about the centre of Cen A. An exception to this trend in velocity can be found at the northern terminus, where Oosterloo & Morganti (2005) have discovered highly turbulent atomic gas.

Radio continuum images reveal huge lobes extending north and south from the galaxy over ∼10°. The radio emission is dominated by synchrotron emission from a jet originating in the active galactic nucleus (AGN) of Cen A and this is driving plasma at relativistic speeds into the surrounding intergalactic medium up to distances of hundreds of kpc. This ongoing interaction results in shock heating of the ISM, clearly visible as extended, knot-like features in X-ray images (Kraft et al. 2003, 2007, 2009; Croston et al. 2009). Although the northern and southern jets exhibit symmetry at large scales, there are crucial differences between them. Both have an inner lobe extending to ∼5 kpc and an outer lobe extending to hundreds of kpc. The difference lies in the existence of a northern middle lobe (NML), which is connected to and powered by the central engine via a large-scale jet (Junkes et al. 1993; Morganti et al. 1999; Hardcastle et al. 2009; Kraft et al. 2009). In contrast, the southern jet appears to terminate at the boundary of the inner southern lobe where it is driving a strong shock into the ISM (Kraft et al. 2003, 2007; Croston et al. 2009).

One aspect of AGN that has come under close scrutiny in recent years is their supposed ability to regulate star formation in the galactic environment by injecting energy into the ISM. This influx of energy prevents atomic gas from cooling and condensing into molecular clouds from which stars would otherwise form (e.g. Silk & Rees 1998). This theoretical mechanism has been invoked to try to recover the apparent discrepancy between the observed population of large, blue galaxies and those predicted by cosmological simulations (Benson 2004; Begelman & Ruszkowski 2005; Binney 2005). Yet it has also been demonstrated that AGN have the ability to *create* stars via the interaction of the jet with gas in the near vicinity of the AGN host galaxy (Rees 1989; van Breugel et al. 2004, and references therein). In terms of affecting a galaxy's evolution, these two phenomena seem to be at odds with one another and clearly the net effect on the galaxy's star formation rate (SFR) will depend on the relative efficiencies of these two processes. Cen A has been the focus of much debate in this respect, with numerous lines of evidence in support of jet-induced star formation taking place in Cen A (Blanco et al. 1975; Graham 1998; Mould et al. 2000; Rejkuba et al. 2002; Oosterloo & Morganti 2005).

Observations of Cen A have recently been extended into the submillimetre with the detection of a cold dust cloud ∼15 kpc north of the nucleus (Stickel et al. 2004). Using the *ISO* observations at 90, 150 and 200 μm, Stickel et al. were able to model a SED applying a single-temperature modified blackbody spectrum ($\beta = 2$), which is typical of thermally emitting cold dust. The resulting fit implied the dust cloud has a very low temperature ($13 \leq T \leq 15.5$ K) and at the distance of Cen A, an inferred dust mass range of $4.5 \leq \log(M_{\rm dust}) \leq 4.9$. Unfortunately the peak of the SED for very cold dust (<15 K) occurs longwards of 200 μm. With only two detections and an upper limit at 90 μm, the fit was constrained to the rising side of the SED. One of the niches that *Herschel* fills, which we exploit in these observations, is that its particular wavelength coverage (70–500 μm) enables observations of both sides of the peak, thus allowing for stricter constraints on the SED fit to the dust thermal emission.

In their discussion of the origin of the cloud, Stickel et al. combined their dust mass with the gas mass estimated from Schiminovich et al. (1994) and Charmandaris et al. (2000) and found that the gas–dust ratio for this cloud is approximately 300. This value falls within the range exhibited by late-type galaxies (Sodroski et al. 1994; Stickel et al. 2000). The ratio of atomic gas to molecular gas is close to unity, which is also consistent with values observed in spirals (Charmandaris et al. 2000). This points towards the late-type galaxy, with which Cen A is believed to have recently merged and which is responsible for the dust and gas in the centre of Cen A, as also being the source of the gas and dust observed in the external ring.

Stickel et al. discuss at length the heating source of this cloud. In particular they focus on the ability of stellar light from Cen A to heat the cloud directly. Temi et al. (2003) developed a model

for predicting the temperature of different types of dust grains at various distances from the centre of early-type galaxies. The model accounts not only for reprocessed stellar emission, but also for electron–grain interactions one would expect in a hot ISM, typical of early-type galaxies. One of the main results was that grains of different sizes are dominated by different heating mechanisms. Small grains (<0.1 μm) are predominantly heated by electron–grain collisions in the hot gas, while large grains (~ 1 μm) are heated by the stellar emission of the evolved stellar population.

This model was then used by Stickel et al. to demonstrate that the temperature of the dust in the northern cloud is fully consistent with the temperature predicted from the Temi et al. model, applied to NGC 4636. Since NGC 4636 is similar in morphology, size and mass to Cen A (Israel 1998), they concluded that the FIR emission is mostly due to dust heated by the ambient starlight from Cen A without the need for heating by other sources such as embedded star formation.

Since their survey field did not encompass the whole H I ring, they were unable to probe the existence of dust elsewhere in the gas ring. Also the resolution of *ISO* was not high enough to allow them to comment on the apparent alignment between the dust and the AGN jet. The superior sensitivity, mapping speed and resolution of *Herschel* present us with the opportunity to map the entire H I ring in the submillimetre to unprecedented levels of sensitivity and detail. For more information on Cen A, Israel (1998) provides a comprehensive review, while Morganti (2010) complements this picture with discoveries that have been made in the interim.

1.2 Very Nearby Galaxy Survey

The Very Nearby Galaxy Survey (VNGS, PI: C. Wilson[1]) is a *Herschel* Guaranteed-Time Key Project focusing on 12 galaxies within 25 Mpc and the archetypal starburst galaxy, Arp 220. The galaxies show a diverse range of masses and properties, from low-mass, late-type galaxies such as NGC 2403 to the large elliptical Cen A, with its energetic active nucleus.

The choice of galaxies was also driven by the wealth of ancilliary data that are available. The design of the survey incorporates both photometry (SPIRE, PACS) and spectrometry (SPIRE-FTS, PACS spectrometer). With such a great breadth of multiwavelength data the survey aims to gain a detailed understanding of the processes that regulate the ISM, and how these processes vary with the environment within different galaxies. The detailed study of these resolved galaxies will not only act as a benchmark for studies of more distant galaxies, but will also bridge the gap between surveys of distant objects and the extensive Galactic surveys which have superior physical resolution but by their nature are limited to observations of one galaxy. Recent results from the VNGS include determining the nature of dust heating in M81 (Bendo et al. 2010), attempting to separate Galactic cirrus emission from extragalactic dust emission in M81 (Davies et al. 2010) and studying the dust distribution and heating mechanisms in and around the starburst galaxy, M82 (Panuzzo et al. 2010; Roussel et al. 2010). While this paper concentrates on the external dust around Cen A, a detailed analysis of the dust within Cen A will be discussed by Parkin et al. (2011).

In Section 2 we detail the *Herschel* observations and the data reduction techniques that were employed. We also give a brief summary of each of the ancilliary data sets that were used in the analysis. In Section 3 we compare multiwavelength images of the clouds as seen with SPIRE, *Spitzer*, *GALEX* and the Australian Telescope Compact Array (ATCA) and show the results of SED fitting to the two dust clouds. In Section 4 we discuss the origin of the dust clouds and the heating mechanisms which are powering the submillimetre emission. Finally in Section 5 we summarize our findings.

2 OBSERVATIONS AND DATA REDUCTION

2.1 Submillimetre observations

The *Herschel* observations of Cen A consist of a $1^\circ \times 1^\circ$ area centred on Cen A itself and mapped by both SPIRE (250, 350 and 500 μm) and PACS (70 and 160 μm) using large scan-map mode. At the time of writing, the PACS data reduction pipeline was optimized for the analysis of the central dust lane in Cen A, rather than the analysis of the dust clouds themselves, hence the regions in the final images surrounding the clouds suffered from degraded surface brightness sensitivity. For these wavelengths MIPS maps (described in Section 2.2) proved to have lower surface brightness limits and so were used in place of PACS.

For the SPIRE observations, the telescope was driven at a scan rate of 30 arcsec s^{-1} and the observations repeated five times. The SPIRE photometer (Griffin et al. 2010) data were processed up to Level 1 (i.e. calibrated bolometer timelines) with a custom made pipeline adapted from the official pipeline.[2] This Jython script was run in the Herschel Interactive Processing Environment (Ott 2010). The purpose of the pipeline is to remove all instrumental artefacts such as glitches, finite bolometer response time, electronic filtering and thermal drift, as well as applying astrometry and flux calibration.

The main difference between our pipeline and the standard one is that we did not run the default temperatureDriftCorrection and the residual, median baseline subtraction. Instead we use a custom method called the BRIght Galaxy ADaptive Element (BriGAdE) to remove the temperature drift. No further baseline subtraction was necessary to bring the bolometer baselines to a common level.

BriGAdE uses the information from the thermistors in each array and directly fits the thermistor data to the entire bolometer timeline (including data where the spacecraft was slewing between scans). If both thermistors exhibited instantaneous 'jumps' (an artefact where a sudden offset is introduced into the timelines) these are either corrected or the comparison switched to the slightly less sensitive dark pixels of the individual array. This approach is hampered slightly by the signal of bright sources in the bolometer timelines. To suppress their influence, they are automatically removed from the fitting process along with samples affected by other artefacts ('jumps' and glitches) in the timelines. When a choice of thermistor is available (i.e. for the 250- and 500-μm arrays), the one providing the best fit is used to subtract a scaled version from the bolometer timelines. This method improves the baseline subtraction significantly, especially in cases where there are large or rapid temperature variations during the observations.

For the final maps, we used the inbuilt naïve mapper of HIPE. The final maps have pixel sizes of 6, 8 and 12 arcsec at 250, 350 and 500 μm, respectively, and instrument-associated noise levels of 5, 5 and 6 mJy $beam^{-1}$.

[1] E-mail: wilson@physics.mcmaster.ca

[2] See Griffin et al. (2008) or Dowell et al. (2010) for a more detailed description of the official pipeline and a list of the individual modules.

2.2 Mid- and far-infrared observations

Cen A was observed with the *Spitzer* observatory using the IRAC and MIPS instruments. We used 24-, 70- and 160-μm MIPS raw data from astronomical observational requests (AORs) 4940288, 4940544 and 4940800 retrieved from the NASA/IPAC Infrared Science Archive to produce the MIPS images. The data from AOR 4940288 were taken at the medium scan rate and cover regions of $\sim 20 \times 50$ arcmin that include the entire optical disc in each waveband. The data from AORs 4940544 and 4940800 were taken at the fast scan rate and cover regions of $\sim 6 \times 115$ arcmin that only cover the jets and the centre of the galaxy. The resulting 160-μm maps from these fast scan data contain gaps, although the 24- and 70-μm data completely cover the field of view.

The data were processed using the MIPS Data Analysis Tools (Gordon et al. 2005) along with additional processing steps described by Bendo et al. (2010) and Bendo et al. (in preparation). The additional processing steps include an additional flat-fielding step for the 24-μm data; the removal of latent images from the 24-μm data; background subtraction in all three wave bands (including zodiacal light subtraction in the 24-μm band and short term drift removal in the 70- and 160-μm bands); and a non-linearity correction applied to the 70-μm data. For the background subtraction to be performed correctly, it is important to identify regions that are not part of the background; we explicitly identified the optical disc and the structures seen in the jets in the SPIRE images as regions to be excluded when calculating background levels.

The full widths at half-maximum (FWHM) of the three MIPS beams are 6 arcsec at 24 μm, 18 arcsec at 70 μm and 38 arcsec at 160 μm. The rms background levels in the final images are 0.0621, 0.463 and 0.553 MJy sr^{-1} at 24, 70 and 160 μm, respectively, and the calibration uncertainties are 4 per cent at 24 μm (Engelbracht et al. 2007), 10 per cent at 70 μm (Gordon et al. 2007) and 12 per cent at 160 μm (Stansberry et al. 2007).

IRAC basic calibrated data frames at 3.6 and 8 μm from AOR 4939008 were taken straight from the NASA/IPAC Infrared Science Archive. The MOPEX software (v18.7.0) was used to interpolate and co-add the individual frames into one large mosaic. The 3.6- and 8-μm FWHMs are 1.7 and 2.0 arcsec, respectively, and the corresponding noise levels in the final mosaicked images are 0.025 and 0.06 MJy sr^{-1}.

As noted in Helou et al. (2004) the 8-μm band contains contributions from both stellar emission and polycyclic aromatic hydrocarbon (PAH) emission. We adopted their technique to isolate the PAH emission: foreground stars were identified by their 3.6–8 μm colours – all unresolved objects with 3.6/8 surface brightness $\gtrsim 4.5$ were masked; the 3.6- and 8-μm images were then multiplied by the aperture correction factors for extended sources (0.944 and 0.737 at 3.6- and 8-μm, respectively); finally the stellar contribution was subtracted from the 8-μm band using the formula

$$I_\nu(\mathrm{PAH}) = I_\nu(8\,\mu\mathrm{m}) - 0.232 I_\nu(3.6\,\mu\mathrm{m}). \quad (1)$$

The final PAH map was then smoothed to the FWHM of the SPIRE 250-μm beam to enhance the extended emission and to allow comparison with the 250-μm map.

2.3 Radio observations

Deep 20-cm continuum and 21-cm spectral line observations of Cen A taken with the ATCA already exist in the literature (20 cm continuum: Morganti et al. 1999; H I: Oosterloo & Morganti 2005; Struve et al. 2010). The authors were kind enough to make the data available for our use and we only summarize the observations here.

The continuum observations were conducted with the ATCA in multiple configurations to maximize the brightness temperature sensitivity while retaining high angular resolution. The on-source time was 12 h in each configuration. The final size of the cleaned beam in the restored image we have used in our analysis is 56 × 26 arcsec^2 (PA = 2°) and the rms noise is 6.7 mJy beam^{-1}.

The H I observations were also conducted using the ATCA using a combination of two configurations. Due to the strength of the continuum source in Cen A, they were restricted in the use of short baselines, which imposed a high-pass filter on the final reduced images. This resulted in all emission on scales larger than 7 arcmin being filtered out. This, however, does not affect our analysis. The size and shape of the restored beam in the final data cube was 29 × 19.5 arcsec^2 (PA = −4.°7). A moment map was produced from the data cube with a 3σ detection limit of 1.0×10^{20} cm^{-2} over a velocity width of 13.2 km s^{-1}. For further details the reader is referred to Morganti et al. (1999) and Oosterloo & Morganti (2005).

2.4 Ultraviolet observations

Cen A was observed by *GALEX* (Martin et al. 2005) as part of the Nearby Galaxy Survey (Gil de Paz et al. 2004). The observations were carried out simultaneously in far-ultraviolet (FUV: $\lambda_{\mathrm{eff}} = 1539$ Å, $\Delta\lambda = 442$ Å) and near-ultraviolet (NUV: $\lambda_{\mathrm{eff}} = 2316$ Å, $\Delta\lambda = 1060$ Å). The images used here were taken from the *GALEX* GR6 data release and have total exposure times of 201 01 and 304 60 s in FUV and NUV.

The final data products consist of circular images ∼1.°2 in diameter with a resolution of 4.5 arcsec (FUV) and 6 arcsec (NUV). The surface brightness limits for the FUV and NUV bands are 30.6 and 29.5 mag arcsec^{-2}, respectively. The reader is referred to Morrissey et al. (2007) for details of the instrument, the observations and data reduction.

3 RESULTS

3.1 SPIRE images

Fig. 1 shows the entire observed field at 250, 350 and 500 μm. The prominent dust lane that seems to cut the galaxy in two at optical wavelengths is clearly seen in emission at submillimetre wavelengths in the centre of the field. The inner radio lobes are clearly visible as extensions perpendicular to the dust disc, particularly in the 350- and 500-μm bands. As stated in the introduction, cold dust peaks longward of 200 μm. This means that the 350- and 500-μm bands are situated well on the Rayleigh–Jeans side of the peak of the blackbody curve. Regions of thermal emission are characterized by decreasing flux levels at increasing wavelengths. From comparing the lobes at the different SPIRE wavelengths, it is clear that they exhibit the opposite emission trend, suggesting that another emission process must be contributing to these longer wavelengths. Synchrotron emission from relativistic electrons spiralling around magnetic field lines in the jet is the most obvious candidate. Synchrotron has a well-characterized spectral slope, α, such that $S \propto \nu^{-\alpha}$ and thus the longer wavelength *Herschel* maps can have significant contributions from synchrotron emission. Synchrotron will be discussed in the Section 3.5 since its presence will adversely affect the SED fitting routine, which only constrains a thermal spectrum.

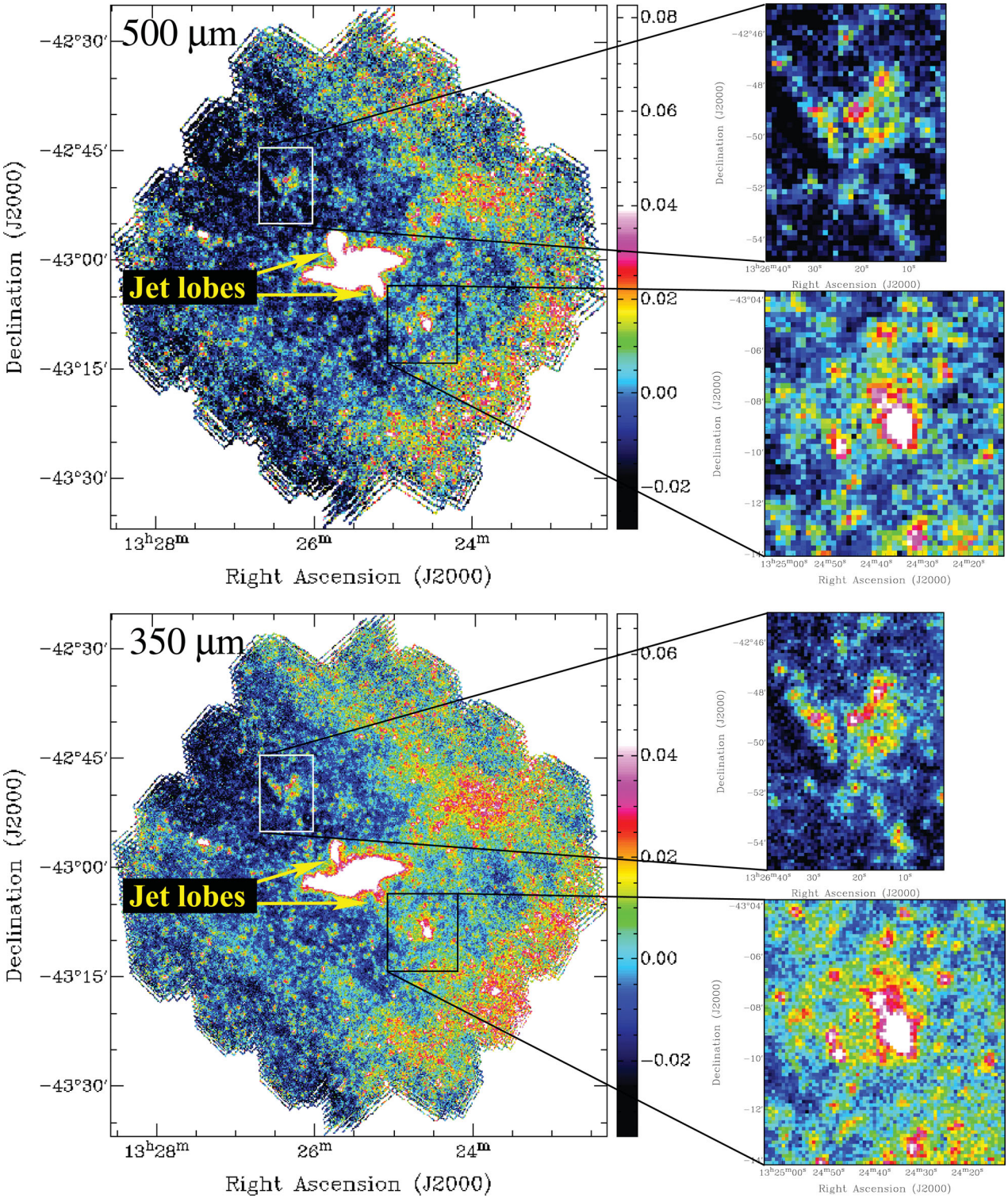

Figure 1. *Herschel*-SPIRE maps of Centaurus A with insets showing the two dust clouds. Top: 500 μm, bottom: 350 μm, over page: 250 μm. The dusty disc of Cen A dominates the emission at the centre of the image. Synchrotron emission from the inner lobes of the AGN jet is visible as extensions north-east and south-west from the centre of the galaxy. All colour bars are in units of Jy beam^{-1}.

Following the line traced by the jets, we see the two clouds: ∼15 arcmin north-east from the centre of Cen A ($13^h26^m18^s.876$, $-42°49'32''$) there is a knot of emission about 4 arcmin across and ∼12 arcmin south-west from the centre of Cen A, ($13^h24^m34^s.976$, $-43°09'02''$) there is another cloud ∼2 arcmin across. Unlike the emission from the inner lobes, the clouds are brighter at shorter wavelengths, suggesting that the sources have a substantial thermal component. The northern cloud is undoubtedly the dust cloud that was detected by Stickel et al. (2004), but the southern cloud, to our knowledge, is a new detection.

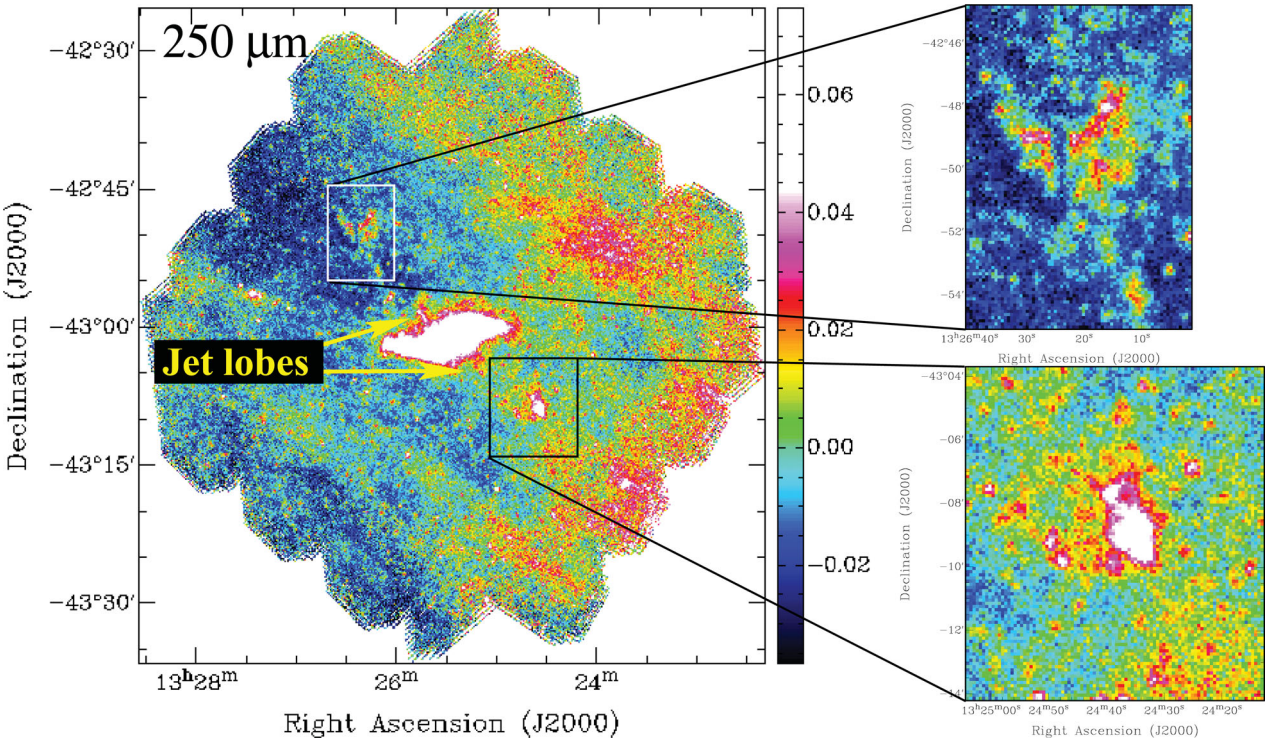

Figure 1 – *continued*

The morphology of the clouds is very different; the southern cloud is fairly smooth with an elliptical shape, whereas the northern cloud is more flocculent and appears to be two smaller clouds separated by a dust-free lane that runs almost perfectly north–south.

The Cen A survey field is large enough that the zero level can be affected by the presence of Galactic cirrus, which introduces gradients across the image. Naturally this complicates our estimates of the background in each region. Under the assumption that the emission is optically thin, the southern cloud could be contaminated with more substantial amounts of Galactic cirrus emission than the northern cloud. This explains why the southern source itself appears brighter, but as we shall see in Section 3.6 the integrated flux of both clouds is actually fairly similar in each band.

3.2 *Spitzer* images

At other wavelengths the clouds show some interesting features. Figs 2–5 illustrate how the mid-infrared (MIR) and far-infrared (FIR) structures compare with those detected in the submillimetre. Each image is a 5–10 arcmin region immediately surrounding each cloud and shows the 250-μm contours overlaid on the images at each individual wavelength. Since 160 μm is close to the peak of the SED for cold dust, one would expect that the morphology exhibited at 250 μm should be similar to that at 160 μm and this is what we find. In Fig. 2 the clouds closely trace the 250-μm emission, although the location of the northern cloud places it close to the edge of the area covered by the MIPS medium scan rate image, hence the area around the northern cloud contains some artefacts related to edge effects at the end of the medium scan rate maps and blank pixels from regions not covered in the fast scan maps. The southern cloud is a strong detection and the extended emission seen at 250 μm is also seen at 160 μm.

If the dust is cold, the spectrum drops off rapidly at wavelengths shorter than ∼160 μm. The expected 70-μm emission is a few orders of magnitude lower than that at 160 μm so a lack of any detection at 70 μm would indicate a cold object. While it seems there is a peak in Fig. 3 at the location of the southern cloud, it happens to be on top of a streak in the image which is a data reduction artefact. Because of this, we consider the southern detection spurious and have only used data from the 70-μm maps to assess upper limits. Using the rms in the vicinity of the clouds leads to an upper limit of ∼200 mJy.

One of the most interesting results to come out of the *Spitzer* Nearby Galaxy Survey was the tight correlation between the 24-μm emission and the atomic hydrogen spectral line emission from Paschen α, Pα (Calzetti et al. 2005, 2007; Prescott et al. 2007; Zhu et al. 2008; Kennicutt et al. 2009). This suggests that the 24-μm band is a particularly good tracer of star-forming regions (although see Bendo et al. 2010 for alternative sources of 24-μm emission). In Fig. 4 we see that both of the clouds show 24-μm emission coincident with the peaks in the 250-μm emission, suggesting a common source for both bands.

Emission from galaxies in the 8-μm band of *Spitzer* is dominated by broad line emission from PAHs. There is also a correlation between the 8-μm PAH emission (corrected for stellar emission) and Pα, however the correlation is not as tight as for 24 μm. The relationship is non-linear and more dependent on metallicity than the 24-μm band, so it is not as reliable to associate 8-μm emission with star formation (e.g. Calzetti et al. 2005; Bendo et al. 2008). Unfortunately the northern cloud falls outside the survey field in the 8-μm band, but the southern field shows some point-like sources embedded in a diffuse, extended cloud. When smoothed to the 250-μm beam, the point sources blend together so that the emission appears as a cloud which closely traces the 250-μm contours, again suggesting a common origin.

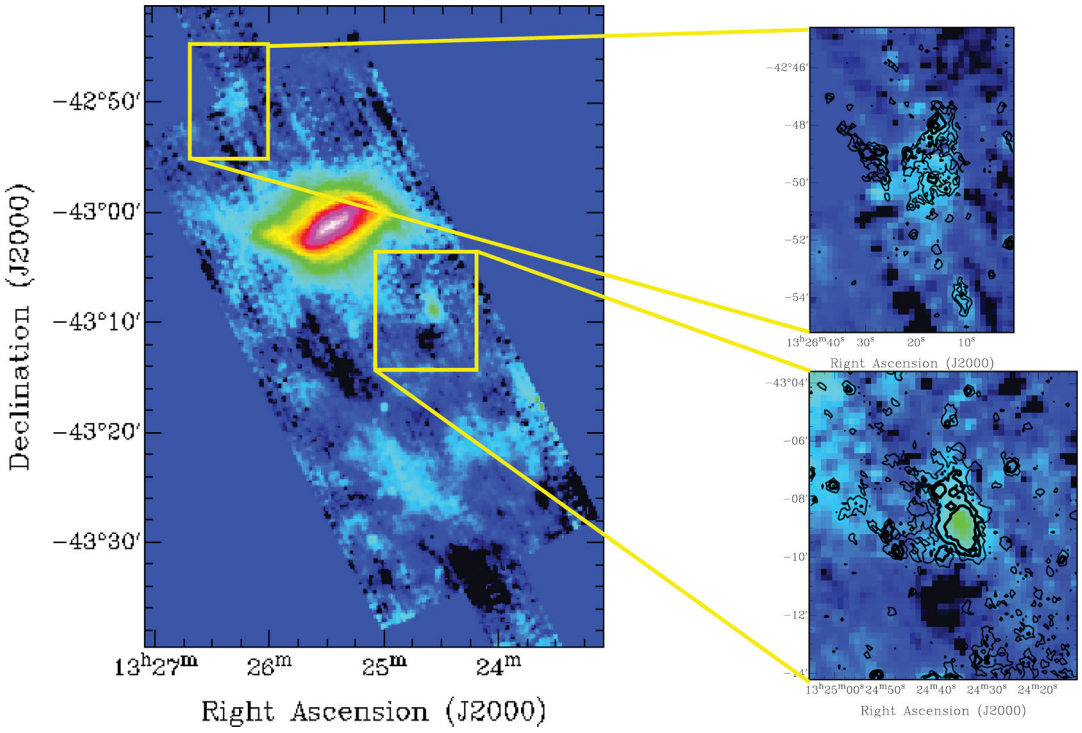

Figure 2. Clockwise from left: *Spitzer* 160-μm map of Cen A region. The colour map has been stretched to enhance diffuse, extended emission. There are a number of visible artefacts, but both dust clouds are visible at the centre of the highlighted regions; the region around the northern cloud with 250-μm contours overlaid at 5, 15, 30 and 50 mJy beam^{-1}; the region around the southern cloud with 250-μm contours overlaid at 15, 30 and 50 mJy beam^{-1}. The 160-μm emission clearly traces the 250-μm emission.

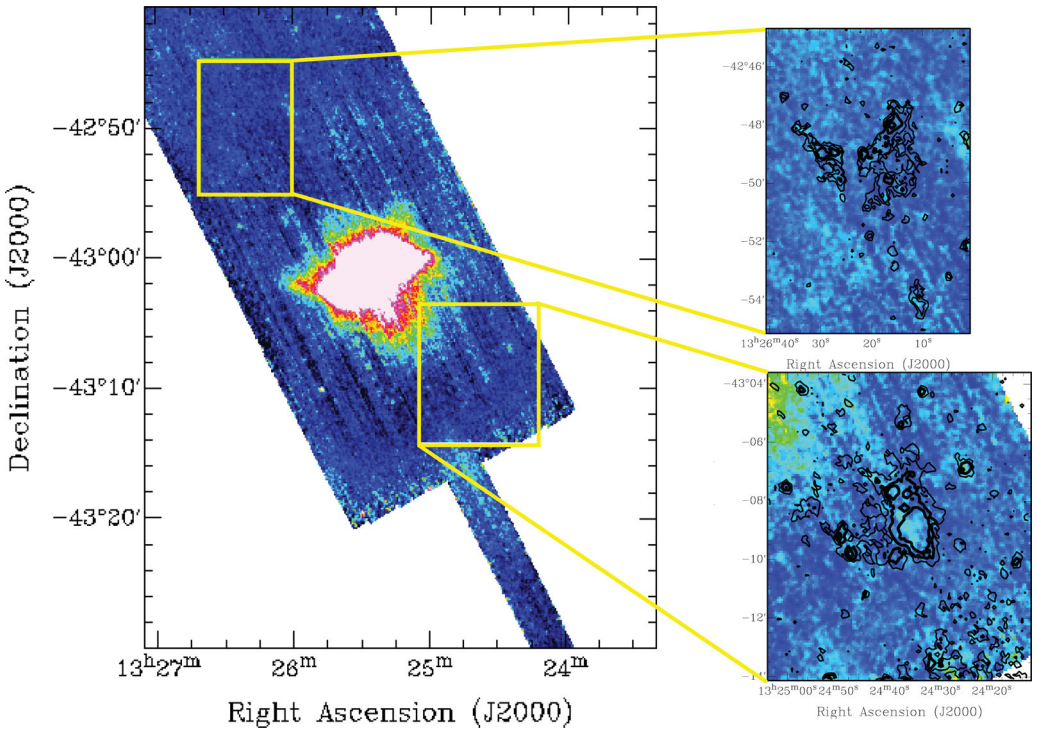

Figure 3. Clockwise from left: *Spitzer* 70-μm map of the Cen A region. The colour map has been stretched to enhance diffuse, extended emission. There are significant stripes present which are artefacts from the observing system that could not be removed during the data reduction process. One of the stripes extends to the position of the southern dust cloud, making flux measurements highly uncertain; the region around the northern cloud with 250-μm contours overlaid at 5, 15, 30 and 50 mJy beam^{-1}; the region around the southern cloud with 250-μm contours overlaid at 15, 30 and 50 mJy beam^{-1}. No 70-μm emission can be unambiguously associated with either cloud.

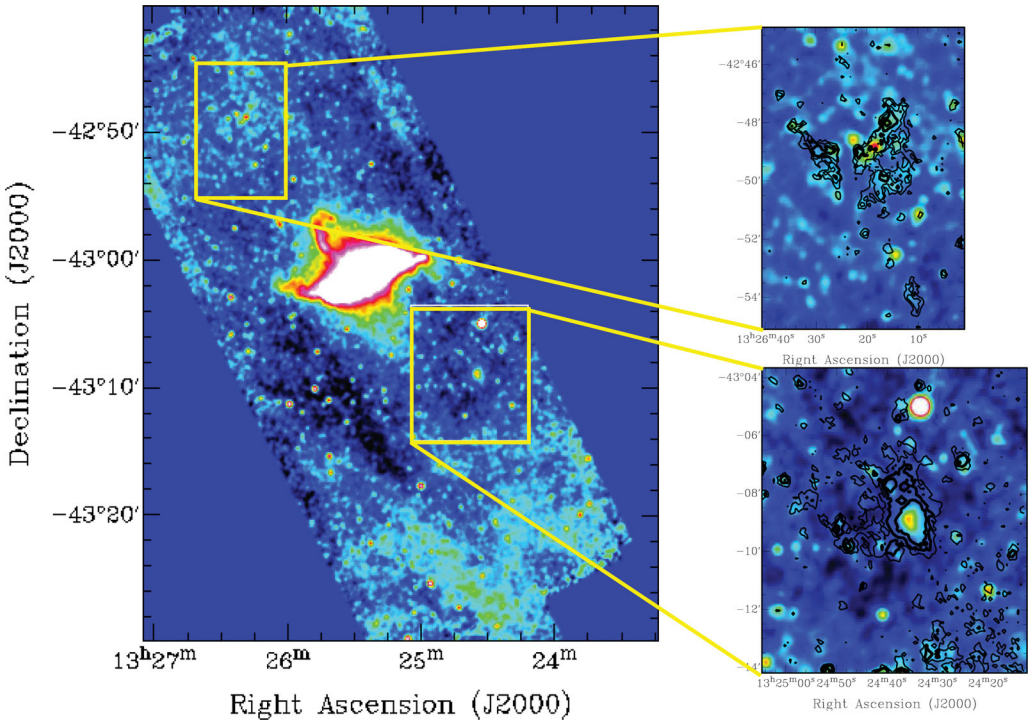

Figure 4. Clockwise from left: *Spitzer* 24-μm map of the Cen A region. The colour map has been stretched to highlight diffuse extended emission. The northern inner lobe of the jet is just visible as are the dust clouds; subimage of the northern dust cloud with SPIRE 250-μm contours overlaid at 5, 15, 30 and 50 mJy beam^{-1}; subimage of the southern dust cloud with 250-μm contours at 15, 30 and 50 mJy beam^{-1}. Both the dust clouds exhibit associated peaks at 24 μm.

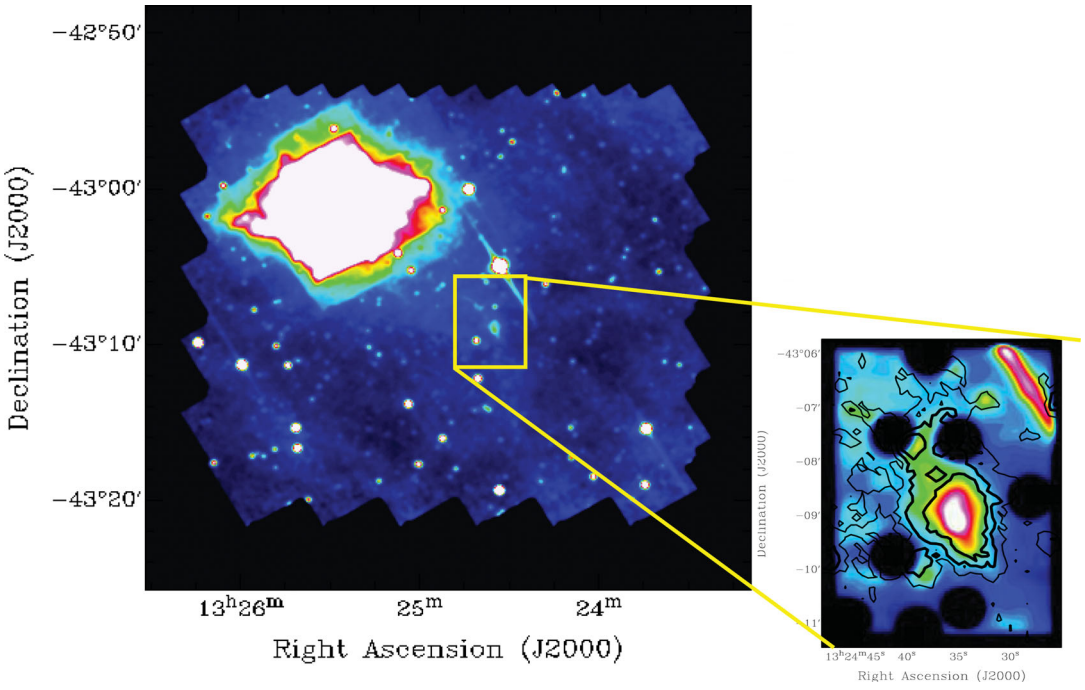

Figure 5. Left: *Spitzer* 8-μm map of the region south-west of Cen A. The colour map has been stretched to enhance diffuse, extended emission. The stellar emission from Cen A dominates the north-eastern corner. The southern dust cloud is visible near the centre of the image; stellar-subtracted 8-μm map of the southern dust cloud with SPIRE 250-μm contours overlaid. The map has been smoothed to the 250-μm beam and the 250-μm contours are: 15, 30 and 50 mJy beam^{-1}. Blank regions indicate foreground stars which have been masked.

3.3 Radio images

Fig. 6 shows the location of the northern jet (white contours) and the H I ring (black contours) overlaid on the 250-μm false colour image. The systemic velocity of the gas is beyond the extent of Galactic H I, which indicates that the gas is part of the Cen A system. The dust emission correlates well with the H I contours, suggesting that the dust is associated with the H I in Cen A as opposed to being

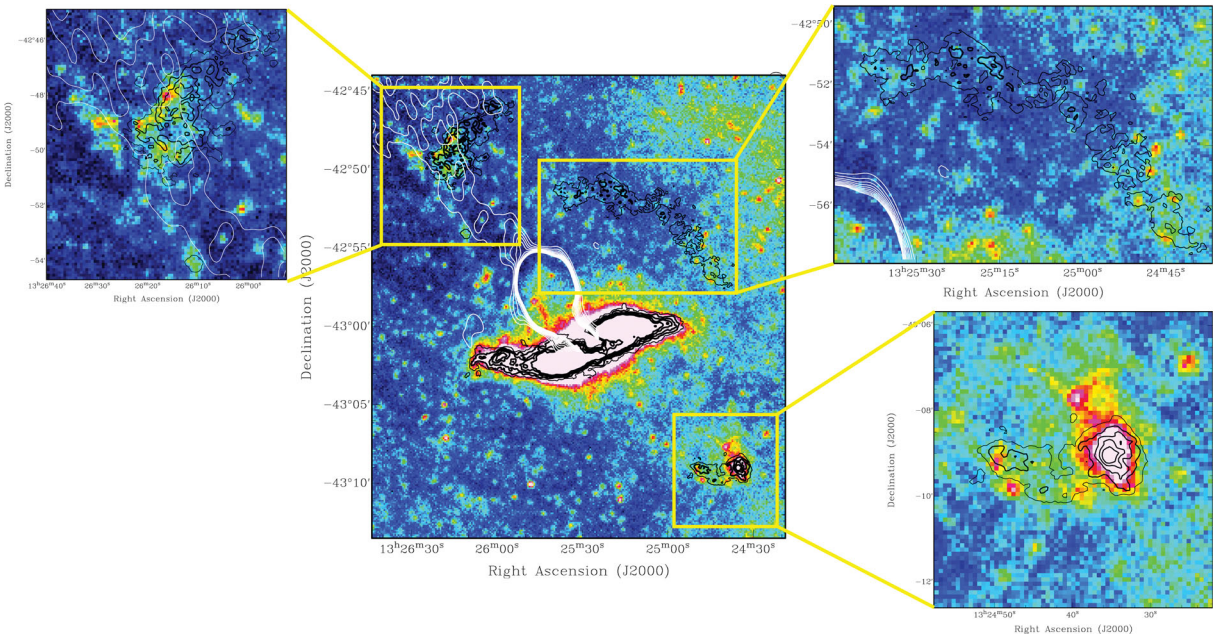

Figure 6. Multiwavelength observations of the immediate surroundings of Cen A. SPIRE 250-μm false colour image with 20-cm continuum emission (white contours) and H I column density (black contours). The image colour scale has been stretched to enhance low surface brightness features, contour levels are as follows: 20 cm – 12.5 × 1, 2, 3, 4, 5, 6, 7, 8 and 9 mJy beam^{-1}; H I – 1, 5, 10, 15 and 20 × 10^{20} cm^{-2}. The image is centred on Cen A and highlights the regions of the H I ring.

a coincidental projection of Galactic cirrus (cf. M81: Davies et al. 2010).

Previous comparisons of the H I velocity dispersion of the southern tip of the northern cloud match the velocity range of ionized gas just to the east of the cloud (Oosterloo & Morganti 2005). This kinematic agreement combined with the spatial coincidence is a good indicator that an interaction is taking place between the jet and the H I cloud. The dust is also coincident with the jet, at least in projection. If the dust is well mixed with the gas, as we would expect, it would imply that the dust is also involved in the jet–cloud interaction. It is also interesting to note that the western part of the H I ring shows no corresponding enhancement in the submillimetre. Possible explanations for this are discussed in Section 4.1.1.

3.4 Ultraviolet images

Both of the *GALEX* images (Figs 7 and 8) have been smoothed to the resolution of the SPIRE 250-μm beam to help bring out some of the more diffuse UV structure. UV emission from the stellar population can be clearly seen in both images. A large amount of emission is present in the eastern half of Fig. 8 which is most likely scattered light from Galactic cirrus. Also striking is the jet-like feature extending from Cen A to the north, far beyond the optical extent of the galaxy. Focusing on the clouds themselves reveals a stark difference between them. The northern cloud clearly has UV emission coincident with it, but the emission is mostly restricted to the edges of the cloud. It may be a chance alignment, but is also what one would expect if the UV emission is embedded within, and obscured by, the dust cloud. The southern cloud, however, shows no sign of UV emission in either of the *GALEX* bands. It is possible that there is no UV originating from the southern dust cloud which would indicate the lack of any star formation in the vicinity. Since UV emission is highly attenuated by dust grains, this could also indicate that UV is present but has been obscured by high column density gas and dust. In the next section, we combine the SPIRE, *Spitzer* and radio data to assess whether the dust cloud emission is purely thermal or contaminated by synchrotron.

3.5 Synchrotron contamination

Since the inner lobe is particularly bright in the 500- and 350-μm image, we must consider whether or not the fluxes are contaminated by synchrotron radiation from the jet. As mentioned in Section 3.1 synchrotron radiation has a power-law emission spectrum. It is therefore possible to estimate the amount of contamination at the SPIRE wavelengths by measuring the clouds' fluxes from lower frequencies (e.g. from radio maps) and extrapolating to the SPIRE wavelengths.

Ideally the spectral index would be measured from a combination of radio maps, but the map of Morganti et al. (1999) is the only radio map with sufficient spatial resolution that extends to the distance of the clouds. In this case we are reduced to assuming a value for the spectral slope. The most extreme case would be to assume that the spectral index is as flat as possible, i.e. $\alpha = 0.5$ (Begelman, Blandford & Rees 1984). We measure a radio flux inside the aperture used for the SED fitting of 270 ± 60 mJy at 1.4 GHz. Even with the flat spectral index this only produces a flux of a few mJy at the 500-μm band. Hence, there is no significant contamination by the jet in the SED of the northern cloud.

To our knowledge no radio maps of sufficient resolution and sensitivity exist for the region covering the southern cloud. Since there is no equivalent to the NML connecting the southern inner lobe to the giant outer lobe, the amount of synchrotron must be even lower than in the northern cloud. Having rejected synchrotron as a possible contaminant we model the fluxes under the assumption that the emission is thermal in origin.

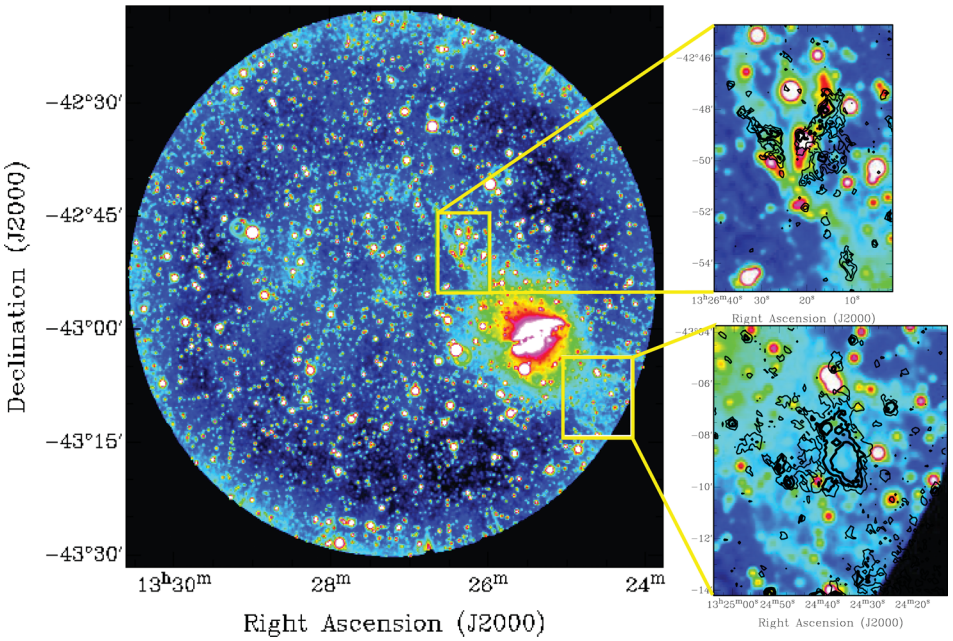

Figure 7. Clockwise from left: *GALEX* NUV map of the Cen A region. The map has been smoothed to the SPIRE 250-μm beam size and the colour scale has been stretched to enhance low surface brightness, extended features. There is a lot of extended emission corresponding to the stellar population of Cen A. A jet-like feature can be seen extending far beyond the stellar radius to the north of Cen A; subimage of the northern dust cloud with SPIRE 250-μm contours overlaid at 5, 15, 30 and 50 mJy beam^{-1}. The region exhibits a large amount of UV coincident with the dust emission; sub-image of the southern dust cloud with 250-μm contours at 15, 30 and 50 mJy beam^{-1}. This dust cloud has no detectable UV emission associated with it.

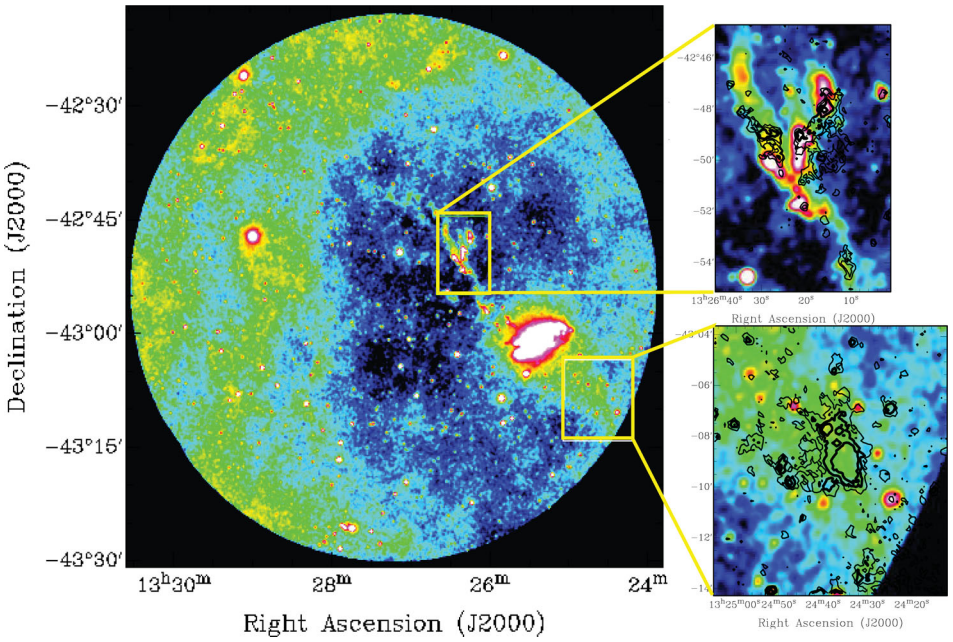

Figure 8. Clockwise from left: *GALEX* FUV map of the Cen A region. The map has been smoothed to the SPIRE 250-μm beam size and the colour scale has been stretched to enhance low surface brightness, extended features. As well as the extended emission from Cen A, Galactic cirrus can be seen in the eastern half of the map. The jet-like feature noticed in the NUV is also visible here; subimage of the northern dust cloud with SPIRE 250-μm contours overlaid at 5, 15, 30 and 50 mJy beam^{-1}. The region exhibits a large amount of UV coincident with the dust emission; subimage of the southern dust cloud with 250 μm contours at 15, 30 and 50 mJy beam^{-1}. This dust cloud has no detectable UV emission associated with it.

3.6 SED fitting

Stickel et al. (2004) fit the FIR SED for the northern cloud using a modified blackbody spectrum, but their analysis was limited to two points on the Wein side of the spectrum (150 and 200 μm) plus another upper limit (90 μm). With so few data points the peak was poorly constrained. With the combination of MIPS and SPIRE data, we now have five points straddling the peak, which should enable us to fit a modified blackbody in the same manner, but with a higher degree of assurance.

Table 1. FIR–submillimetre flux measurements for the two dust clouds. Uncertainties are shown in brackets and are 20 per cent for SPIRE fluxes and 30 per cent for *Spitzer* measurements.

Cloud	S_{500} Jy	S_{350} Jy	S_{250} Jy	S_{160} Jy	S_{70} Jy
North	0.33 (0.07)	0.8 (0.2)	0.8 (0.2)	0.7 (0.1)	< 0.2
South	0.37 (0.07)	0.9 (0.2)	1.0 (0.2)	1.5 (0.5)	< 0.2

We adopted the SED fitting routine as used in Smith et al. (2010), in which the uncertainties in the fitted dust mass and temperature are derived from several thousand Monte Carlo simulations. The benefit of the simulations is the determination of the error distributions for the mass and temperature which are not necessarily Gaussian, thus lending a higher degree of robustness to the quoted uncertainties. The fitting routine allows the user to specify the emissivity index, β as a free parameter, but we found that the simulations did not converge, so β was fixed at 2. The dust mass-opacity coefficient used was 0.192 m^2 kg^{-1} at 350 μm (Li & Draine 2001).

Before fitting the SED, the images were smoothed to the resolution of the SPIRE 500-μm beam. An aperture was defined for each cloud based on the highest signal-noise map (250 μm) and these apertures were used across all bands. The lack of coverage in the 160-μm image in the north limited our ability to measure flux over the whole cloud, but only a small section of the eastern-most part of the cloud was lost and it is unlikely to make a significant difference to the final result.

The measured fluxes are shown in Table 1. Quoted uncertainties are larger than the nominal calibration uncertainties for each instrument, but given the amount of foreground contamination against which the fluxes were measured, we feel these larger error bars are justified. It was apparent that even after smoothing, the quality of the 70-μm images was only good enough to provide upper limits, but this still gave stricter constraints than omitting the 70-μm data altogether.

The SEDs for the dust clouds are presented in Fig. 9. The SED for the northern cloud compares well with the SED of Stickel et al. (2004), and we derive a similar dust temperature: $T = 12.6^{+1.1}_{-1.2}$ K. We recover more mass than Stickel et al., $\log(M_{\rm dust}/{\rm M}_\odot) = 5.8^{+0.2}_{-0.2}$, most likely because of the increased wavelength coverage provided by *Herschel*. For the southern cloud we measure a dust mass and temperature of $\log(M_{\rm dust}/{\rm M}_\odot) = 5.6^{+0.2}_{-0.2}$, $T = 15.1^{+1.7}_{-1.6}$ K. Combining the dust masses with the gas masses measured by Charmandaris et al. (2000), we derive gas–dust ratios of 121 and 110 which are typical of late-type, star-forming galaxies. Having established a thermal origin for the submillimetre emission in these clouds, we now discuss their origin and heating mechanisms.

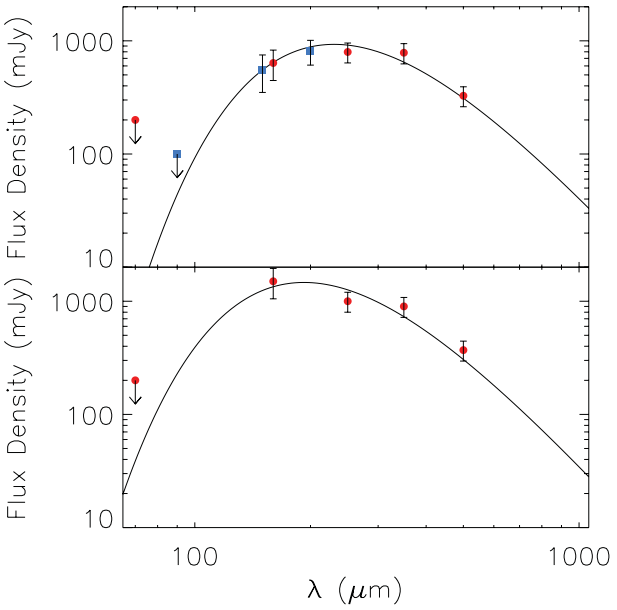

Figure 9. Modified blackbody, single-temperature fits to the FIR–submillimetre data assuming a $\beta = 2$ emissivity. Data points from this analysis are shown as red dots and the data points of Stickel et al. are shown as blue squares. Arrows indicate upper limits. Top: northern cloud. Bottom: southern cloud.

4 DISCUSSION

4.1 Origin of the clouds

4.1.1 Galaxy merger

A comparison of the distribution of the atomic gas and the dust (Fig. 6) reveals that the only detected dust emission that can be unambiguously associated with the H I ring is at the position of the two clouds. The lack of submillimetre emission in the rest of the gas ring has three possible explanations: either there is no dust in other parts of the ring, or the column density of dust falls below the SPIRE detection limit, or the dust is present but too cold to emit at the SPIRE wavelengths.

If the galaxy that merged with Cen A was a late type, it would be expected that the dust is well mixed with the gas in the H I ring. It is unlikely, therefore, that there is no dust anywhere else in the orbiting gas. This then leaves the question of whether the dust is too diffuse or too cold.

Assuming that the dust in the H I cloud to the west is at the same temperature as the two detected clouds, the SPIRE detection limit can be used to estimate the limiting column density of dust within it. Apertures were used to define the local rms in the vicinity of the cloud and this was adopted as the noise level. The source region was defined from the H I map of Struve et al. (2010), using an H I column density of 10^{19} cm^{-2}. The 500-μm map was the most sensitive in the region of the western cloud. Despite having a slightly larger instrumental noise value, this wavelength is less sensitive to Galactic cirrus which dominates the background in this region. The rms pixel value in the vicinity of the H I cloud was 10.1 mJy $beam^{-1}$. This gave a 3σ flux upper limit of 66.6 mJy over the extent of the cloud. For a 14 K cloud with $\beta = 2$, this resulted in an upper limit for the dust mass of $M_{\rm dust} < 9.4 \times 10^5$ $M_\odot$, or a corresponding gas-dust ratio of $M_{\rm gas}/M_{\rm dust} > 63$. This is not a particularly strong lower limit for the gas–dust ratio, and suggests that the dust is simply too diffuse to be detected by SPIRE. Without a strong upper limit on the gas–dust ratio there is little use in exploring the impact of a significant amount of colder dust in the western H I cloud.

These findings are consistent with having dust well mixed throughout the gas ring and the gas–dust ratio is typical of late-type galaxies as is the ratio of the atomic to molecular gas. This supports the scenario that the dust and gas originated in the galaxy that merged with Cen A to form the dusty disc at the centre of Cen A.

The northern cloud is coincident with the high-velocity H I gas which has been linked to the jet-induced star-forming region nearby. Opportunities to explore jet-induced star formation in the kind of detail that Cen A offers are rare, so it is interesting to explore

the possibility that this local star formation is responsible for the existence of the northern dust cloud.

4.1.2 Jet-induced star formation

If the dust originated from the stars in the vicinity of the clouds, we can use a simple argument to determine whether or not the SFRs are sufficiently high to have formed the mass of dust we observe. Stardust is formed in the cool, stellar winds of low–intermediate mass stars (LIMS) on time-scales of 0.5–1 Gyr and in supernovae (SNe) on time-scales of tens of Myr. In the Milky Way, the major dust source is presumed to be the former, with LIMS injecting dust at a rate of $\sim 2 \times 10^{-3}\,\mathrm{M_\odot\,yr^{-1}}$ (e.g. Whittet 2003). Recent FIR observations of Galactic and extragalactic SN remnants with *Spitzer* and *Herschel* (e.g. Rho et al. 2008; Barlow et al. 2010; Otsuka et al. 2010) suggest SNe contribute a dust mass-loss rate of $<1 \times 10^{-3}\,\mathrm{M_\odot\,yr^{-1}}$ (corresponding to $<0.1\,\mathrm{M_\odot}$ of dust formed per SNe). However, as SN shocks are also responsible for destroying dust in the ISM via sputtering, it is not yet clear how much of the dust observed in remnants survive their journey into the ISM.

We can estimate the stellar dust injection rate needed to produce the observed dust mass in the Cen A clouds by comparing the rate at which dust grains are destroyed in the ISM. The time-scale for dust destruction can be estimated using (McKee 1989):

$$t_{\mathrm{des}} = \frac{M_{\mathrm{d}}}{R_{\mathrm{SN}} M_{\mathrm{d,s}}} = \frac{M_{\mathrm{d}}}{0.05\mathrm{SFR}}, \quad (2)$$

where M_{d} is the dust mass, R_{SN} is the SN rate, $M_{\mathrm{d,s}}$ is the mass of dust shocked and destroyed by one SN blast wave ($\sim 3\,\mathrm{M_\odot}$ for shocks with speeds $v > 100\,\mathrm{km\,s^{-1}}$ – Dwek & Cherchneff 2011). Using equation (2), dust is destroyed on time-scales of $\tau_{\mathrm{des}} \sim 400\,\mathrm{Myr}$ in the Milky Way (Jones et al. 1994; Tielens 1998). The estimate requires knowledge of the SFR, and a number of prescriptions exist to estimate the SFR for the northern cloud based on its luminosity at 24 μm, NUV and FUV. For completeness the SFRs for the southern cloud are also calculated, but the reader is reminded that there is no evidence of a connection between the southern jet and this dust cloud so in this case the assumed star formation is not jet induced.

Using the prescription in Relaño et al. (2007) as presented by Calzetti et al. (2010) the northern cloud exhibits $S_{24} = 9\,\mathrm{mJy}$, which corresponds to a $\mathrm{SFR_{24}} = 1.4 \times 10^{-3}\,\mathrm{M_\odot\,yr^{-1}}$; For the southern cloud we measure $S_{24} = 7\,\mathrm{mJy}$. This corresponds to a $\mathrm{SFR_{24}} = 1.2 \times 10^{-3}\,\mathrm{M_\odot\,yr^{-1}}$.

Iglesias-Páramo et al. (2006) provide recipes for calculating SFRs in the UV bands of *GALEX*. The UV luminosities must first be corrected for Galactic extinction. Galactic extinction magnitudes, $E(B-V)$, were provided by the *GALEX*, MAST website using objects identified close to (<30 arcsec) the cloud positions within the Cen A field. For the northern cloud $E(B-V) = 0.102$ and for the southern cloud $E(B-V) = 0.138$. The conversion from A_B to A_{UV} was calculated using the method described in Wyder et al. (2007). The attenuation values are $A_{\mathrm{UV}} = 0.840$ for the northern cloud and $A_{\mathrm{UV}} = 1.055$ for the southern cloud. The measured NUV and FUV magnitudes were then corrected by these values.

For the southern cloud, the 5σ limits based on the error in the background estimates, corrected for Galactic extinction, were used to provide upper limits. The extinction-corrected luminosities were then used to calculate the SFRs. For the northern cloud we derive a $\mathrm{SFR_{FUV}} = 3.8 \times 10^{-3}\,\mathrm{M_\odot\,yr^{-1}}$ and $\mathrm{SFR_{NUV}} = 2.4 \times 10^{-3}\,\mathrm{M_\odot\,yr^{-1}}$; for the southern cloud $\mathrm{SFR_{FUV}} < 2 \times 10^{-4}\,\mathrm{M_\odot\,yr^{-1}}$ and $\mathrm{SFR_{NUV}} < 5 \times 10^{-5}\,\mathrm{M_\odot\,yr^{-1}}$. All the luminosity measurements and associated SFRs are shown in Table 2. For reference, the SFR derived from Mould et al. (2000) is also shown.

Table 2. IR and UV star formation rates for the dust clouds.

Cloud	North	South
S_{24} (Jy)	0.009	0.007
L_{24} ($\times 10^{39}$erg s^{-1})	1.69	1.36
$\mathrm{SFR_{24}}$($\mathrm{M_\odot\,yr^{-1}}$)	0.00143	0.0012
m_{NUV}	15.3	>20.96
m_{FUV}	16.1	>19.06
$E(B-V)$	0.102	0.128
L_{NUV} ($\times 10^{40}$erg s^{-1})	5.92	<0.06
L_{FUV} ($\times 10^{40}$erg s^{-1})	4.21	<0.15
$\mathrm{SFR_{NUV}}$ ($\mathrm{M_\odot\,yr^{-1}}$)	0.0024	$<5 \times 10^{-5}$
$\mathrm{SFR_{FUV}}$ ($\mathrm{M_\odot\,yr^{-1}}$)	0.0038	$<2 \times 10^{-4}$
$\mathrm{SFR_{M00}}$ [a] ($\mathrm{M_\odot\,yr^{-1}}$)	0.0012	–

[a]Mould et al. (2000) based on a the maximum age of detected OB associations and total number of detected OB associations assuming a Salpeter mass function.

The SFR values for the northern cloud as judged from four independent tracers differ by factors of a few. The SFRs broadly agree, given the different caveats and scatter that are associated with each SFR estimator. The low SFR for the northern cloud implies dust in this environment could survive for 2 Gyr. The dust injection rate from stars for this cloud would therefore need to be $M_{\mathrm{d}}/\tau_{\mathrm{des}} \sim 10^{-4}\,\mathrm{M_\odot\,yr^{-1}}$ to produce the total dust mass. From the low SFR ($\sim 10^{-3}\,\mathrm{M_\odot\,yr^{-1}}$), we would expect a dust injection rate from LIMS and SNe (scaled from the Milky Way parameters and SFR) of $10^{-5}\,\mathrm{M_\odot\,yr^{-1}}$; this is an order of magnitude lower than required. At this rate, it would take more than 30 Gyr to build up the $4 \times 10^5\,\mathrm{M_\odot}$ of dust observed by *Herschel* with a stellar mass-loss source of dust.

The dust clouds detected here cannot be explained by replenishment of the dust via stellar mass-loss; the destruction time-scales would need to be more than an order of magnitude longer than currently estimated and the induced star formation would need to be replenishing dust for an unfeasibly long time. This reinforces the notion that the dust most probably originated in the galaxy that merged with Cen A and was redistributed along with the gas as the galaxy was torn apart.

Simulations of merger events have demonstrated that the gas and dust are preferentially stripped, so the lack of a stellar enhancement in the H I ring is not unusual. It does, however, raise the question of what possible heating source could be responsible for heating the clouds to produce their submillimetre emission.

4.2 Dust heating mechanisms

The dust clouds reside in a complex environment. They exist on the very outskirts of the stellar extent of Cen A and heating by the stellar population will have some effect. The region around Cen A is also rich in X-ray emission and the northern cloud appears to lie in the projected path of the AGN jet and also close to the beam of ionizing radiation discovered by Morganti et al. (1991). We now consider each of these heating mechanisms and discuss their relative contribution.

4.2.1 Heating by aging stars

The model of Temi et al. (2003) predicts temperatures of dust grains of different sizes as a function of radius for early type galaxies such as Cen A. The model environment consisted of X-rays from a hot ($>10^7$ K) ISM and starlight from the evolved stellar population. From fig. 2 of Temi et al. (2003) the expected dust temperature at the distance of the dust clouds is 14–16 K for grains of size $\sim$1 μm, which is entirely consistent with our measurements and also the previous measurement of Stickel et al. (2004). For smaller grains, the temperature profiles are too high to account for the low temperatures we see, so the clouds must be dominated by large grains if the Temi model is representative of the grain population. The temperature profiles from grains of this size are dominated by heating from the aging stars, with electron heating becoming more important for smaller grains. From this we infer that the clouds are most likely heated by the old stellar population.

It is curious that in such a complicated environment, a single heating mechanism can account for the grain heating. We now examine the alternative possible mechanisms and attempt to explain why they are not credible.

4.2.2 Beamed radiation

Ionization of the material close to the dust clouds in Cen A by a beamed nuclear source was first proposed by Morganti et al. (1991, 1992). Through extensive modelling incorporating multicloud photoionization, they were able to reject other scenarios such as heating from a diffuse X-ray halo or cosmic ray heating in favour of the beamed, ionizing photons, emanating from a source embedded deep within the obscured nucleus of Cen A. We have used their estimate of ionizing photon flux to calculate the temperature of a dust grain at the distance of the clouds.

In the absence of attenuation, the total energy incident on a grain is simply given by

$$Q_{\rm heat} = q h \nu_{\rm H\alpha} \Omega_{\rm grain}, \quad (3)$$

where q is the ionizing photon flux (photons s^{-1} sr^{-1}), $h\nu_{\rm H\alpha}$ is taken as an estimate of the minimum energy of the ionizing photons and $\Omega_{\rm grain}$ is the solid angle of a single grain ($\sim 3.3 \times 10^{-55}$ sr) at the distance of the dust clouds ($\sim$15 kpc).

This incident power is then absorbed completely by the grain, and radiated away:

$$Q_{\rm cool} = 4\pi a_{\rm X}^2 \sigma_{\rm SB} T_{\rm d}^4 \langle Q_{\rm abs} \rangle, \quad (4)$$

where $a_{\rm X}$ is the cross-sectional area of a grain (a spherical grain diameter of 1 μm is assumed) and $Q_{\rm abs}$ is the absorption co-efficient and we use the approximation $Q_{\rm abs} \approx 1.35 \times 10^{-5} T_{\rm d}^2 a_{\rm X}$ following Temi et al. (2003) and Draine & Lee (1984).

By conservation of energy, equations (3) and (4) must balance. So if one knows q, it is possible to calculate T. Morganti et al. (1991) calculate a value of $q = 10^{53}$ photons s^{-1} sr^{-1} to account for the Hα luminosity in the filaments. With this incident photon flux, it is possible to raise the grains to 67 K. Since the dust temperature is such a weak function of the incident power, one would only require $\sim$0.01 per cent of power from the beamed flux in order to raise the dust temperature to $\sim$14 K. While this is plausible, the beamed flux would have to have a sufficient opening angle to illuminate both dust clouds entirely. The northern cloud is roughly 5 kpc across and at the distance of the cloud (15 kpc) this would require that the photon beam have an opening angle of at least $\sim 20^\circ$. This is uncomfortably large for a beamed source and we note that this minimum estimate does not engulf the optical filaments to the east. Also there is no known evidence of optical filaments to the south of Cen A, suggesting that the ionizing beam cannot be interacting with the southern cloud at all.

4.2.3 X-ray heating

X-ray observations of Cen A have revealed that the galaxy has an X-ray jet and exists inside a diffuse X-ray halo (Feigelson et al. 1981; Turner et al. 1997; Kraft et al. 2009). The model of Temi et al. (2003) takes into account the effects of a diffuse X-ray medium in which the dust grains are situated, and has been found to impact only small ($<$0.1 μm) grains. It is possible that the presence of discrete X-ray sources might have a more significant effect.

In a recent study, Kraft et al. (2009) reported the discovery of several bright X-ray knots on the eastern edge of the NML, which places them to the north and east of the northern dust cloud. The nearest X-ray knot to the northern cloud (N4 in the notation of Kraft et al.) has a luminosity of only $\sim 5 \times 10^4$ L$_\odot$ and therefore cannot be a potential heating source.

A sufficiently bright low-mass X-ray binary would also have the potential to heat the cloud. From figs 2 and 3 in Kraft et al. there are two compact X-ray sources close to the location of the dust clouds. Using the *XMM–Newton* archive the two sources were located in the original data and found to have luminosities of $L_{\rm X}$(north) $= 2.9 \times 10^{37}$ erg s^{-1} and $L_{\rm X}$(south) $= 3.6 \times 10^{36}$ erg s^{-1}. The luminosities are orders of magnitude below that required to power the dust clouds, so we conclude that X-ray emission by either diffuse hot gas or compact sources is not strong enough to account for the observed luminosity in the submillimetre.

4.2.4 Jet mechanical heating

The final situation to consider is a direct interaction between the radio jet and the dust cloud. In their comparison of the jet power to the X-ray power of the bright knots, Kraft et al. (2009) estimate that the jet itself has a mechanical power of 6×10^{42} erg s^{-1}. Fig. 6 indicates that the jet forms a cylinder from the north-eastern inner lobe to the NML. If it is assumed that the power is uniformly distributed, then it is possible to estimate the amount of mechanical power deposited into a single grain and hence deduce the dust grain temperature using equation (4).

We approximate the jet as a cylinder $\sim$4 arcsec in diameter, which at the distance of Cen A is equivalent to $\sim$4.2 kpc. The cross-section of the cylinder at the distance of the northern dust cloud ($\sim$15 kpc) as seen from the nucleus of Cen A subtends an angle of $\sim 16^\circ$. Hence the jet subtends a solid angle of $\sim$0.005 sr at the distance of the northern dust cloud. This gives the jet a flux density of $\sim 1.2 \times 10^{45}$ erg s^{-1} sr^{-1}. This equates to $\sim 3.6 \times 10^{-10}$ W per grain. Balancing this power with equation (4) yields a dust temperature of $\sim$2600 K. If all the mechanical energy were dumped into the dust, the dust would not survive, so the transfer of jet mechanical energy would have to be incredibly inefficient. The southern cloud also poses a problem for this mechanism, since there is no evidence of a jet–cloud interaction in the region surrounding the southern cloud. Despite the striking alignment between the dust clouds and the jet, the jet appears to have little influence on the dust, suggesting that the alignment is purely a projection effect.

We come to the same conclusion as Stickel et al. (2004). The simplest scenario that satisfactorily explains the origin of the dust is one in which the dust and gas in the clouds were once part of the

late-type galaxy that merged with Cen A to produce its prominent dust lane. The only heating source that can account for the observed temperatures in both of the clouds is heating from the starlight of the evolved stellar population within Cen A.

5 CONCLUSIONS

The results of these *Herschel*-SPIRE observations of Cen A have revealed two dust clouds external to Cen A and co-aligned with the axis of the AGN jet. The northern cloud lies at a projected distance of ∼15 kpc from the centre of Cen A and has been previously detected, while the southern cloud, at a distance of ∼12 kpc, is a new detection in the submillimetre. We have used SED analysis and a single-temperature, modified blackbody spectrum to fit the *Herschel*-SPIRE data and reprocessed MIPS data. The resulting fits show that the two clouds are thermal in origin and have roughly the same dust temperature and mass: $T_{\rm north} = 12.6^{+1.1}_{-1.2}$ K, $T_{\rm south} = 15.1^{+1.7}_{-1.6}$ K; $\log(M_{\rm north}/{\rm M}_\odot) = 5.8^{+0.2}_{-0.2}$, $\log(M_{\rm south}/{\rm M}_\odot) = 5.6^{+0.2}_{-0.2}$. The measured values for the northern cloud are consistent with previous measurements based on *ISO* data (Stickel et al. 2004).

The clouds reside at the termini of the partial H I ring that surrounds Cen A where the H I column density is highest. The measured gas–dust ratios and H I/H_2 ratios are typical of a late-type gas-rich galaxy, which support the hypothesis that the dust and gas originated in the galaxy which has since merged with Cen A to form its dusty disc. Dust was not unambiguously detected in other parts of the H I ring and we attribute this to the dust having a column density below the SPIRE detection threshold rather than having a lower temperature or an absence of dust altogether.

The dust clouds have also been detected in H I, CO, 24 μm and the southern cloud, at least, also exhibits 8 μm PAH emission. SFRs have been calculated based on UV–FIR tracers but the SFRs are too low to have produced the inferred mass of dust in a reasonable time frame. The low SFRs and the lack of UV emission in the southern cloud imply that the dust emission is unrelated to star formation. Dust heating by the evolved stellar population is the simplest mechanism capable of explaining the observed temperatures for both clouds. The jet therefore is unlikely to play a major role in the heating process and its alignment with the clouds is purely coincidental.

ACKNOWLEDGMENTS

SPIRE has been developed by a consortium of institutes led by Cardiff University (UK) and including Univ. Lethbridge (Canada); NAOC (China); CEA, LAM (France); IFSI, Univ. Padua (Italy); IAC (Spain); Stockholm Observatory (Sweden); Imperial College London, RAL, UCL-MSSL, UKATC, Univ. Sussex (UK); and Caltech, JPL, NHSC, Univ. Colorado (USA). This development has been supported by national funding agencies: CSA (Canada); NAOC (China); CEA, CNES, CNRS (France); ASI (Italy); MCINN (Spain); SNSB (Sweden); STFC (UK) and NASA (USA). HIPE is a joint development (are joint developments) by the Herschel Science Ground Segment Consortium, consisting of ESA, the NASA Herschel Science Center, and the HIFI, PACS and SPIRE consortia.

REFERENCES

Baade W., Minkowski R., 1954, ApJ, 119, 215
Barlow M. J. et al., 2010, A&A, 518, L138
Begelman M. C., Ruszkowski M., 2005, Phil. Trans. R. Soc. Lon. A, 363, 655
Begelman M. C., Blandford R. D., Rees M. J., 1984, Rev. Modern Phys., 56, 255
Bendo G. J. et al., 2008, MNRAS, 389, 629
Bendo G. J. et al., 2010, MNRAS, 402, 1409
Benson A. J., 2004, in Diaferio A., ed., Proc. IAU Colloq. 195, Outskirts of Galaxy Clusters: Intense Life in the Suburbs. Cambridge Univ. Press, Cambridge, p. 527
Bicknell G. V., 1991, Proc. Astron. Soc. Aust., 9, 93
Binney J., 2005, Phil. Trans. R. Soc. Lon. A., 363, 739
Blanco V. M., Graham J. A., Lasker B. M., Osmer P. S., 1975, ApJ, 198, L63
Calzetti D. et al., 2005, ApJ, 633, 871
Calzetti D. et al., 2007, ApJ, 666, 870
Calzetti D. et al., 2010, ApJ, 714, 1256
Charmandaris V., Combes F., van der Hulst J. M., 2000, A&A, 356, L1
Chattopadhyay A. K., Chattopadhyay T., Davoust E., Mondal S., Sharina M., 2009, ApJ, 705, 1533
Croston J. H. et al., 2009, MNRAS, 395, 1999
Davies J. I. et al., 2010, MNRAS, 409, 102
Dowell C. D. et al., 2010, in Oschmann J. M., Jr, Clampin M. C., MacEwen H. A., eds, SPIE Conf. Ser. Vol. 7731, Space Telescopes and Instrumentation 2010: Optical, Infrared and Millimeter wave. 773136, SPIE, Bellingham
Draine B. T., Lee H. M., 1984, ApJ, 285, 89
Dwek E., Cherchneff I., 2011, ApJ, 727, 63
Engelbracht C. W. et al., 2007, PASP, 119, 994
Feigelson E. D., Schreier E. J., Delvaille J. P., Giacconi R., Grindlay J. E., Lightman A. P., 1981, ApJ, 251, 31
Fragile P. C., Murray S. D., Anninos P., van Breugel W., 2004, ApJ, 604, 74
Gil de Paz A., Madore B. F., Boissier S., BAAS, 36, 1410
Gordon K. D. et al., 2005, PASP, 117, 503
Gordon K. D. et al., 2007, PASP, 119, 1019
Graham J. A., 1998, ApJ, 502, 245
Griffin M. J. et al., 2008, in Oschmann J. M., Jr, Clampin M. C., MacEwen H. A., eds, SPIE Conf. Ser. Vol. 7010, Space Telescopes and Instrumentation 2008: Optical, Infrared and Millimeter. 70102Q, SPIE, Bellingham
Griffin M. J. et al., 2010, A&A, 518, L3
Hardcastle M. J., Cheung C. C., Feain I. J., Stawarz L., 2009, MNRAS, 393, 1041
Helou G. et al., 2004, ApJS, 154, 253
Herschel Sir J. F. W., 1847, Results of Astronomical Observations Made During the Years 1834, 5, 6, 7, 8, at the Cape of Good Hope; being the completion of a telescopic survey of the whole surface of the visible heavens, commenced in 1825. Smith, Elder and Co., London
Iglesias-Páramo J. et al., 2006, ApJS, 164, 38
Israel F. P., 1998, ARA&A, 8, 237
Jones A. P., Tielens A. G. G. M., Hollenbach D. J., McKee C. F., 1994, ApJ, 433, 797
Junkes N., Haynes R. F., Harnett J. I., Jauncey D. L., 1993, A&A, 269, 29
Kraft R. P., Vázquez S. E., Forman W. R., Jones C., Murray S. S., Hardcastle M. J., Worrall D. M., Churazov E., 2003, ApJ, 592, 129
Kraft R. P. et al., 2007, ApJ, 665, 1129
Kraft R. P. et al., 2009, ApJ, 698, 2036
Li A., Draine B. T., 2001, ApJ, 554, 778
McKee C., 1989, in Allamandola L. J., Tielens A. G. G. M., eds, Proc. IAU Symp. 135, Interstellar Dust. p. 431, Kluwer, Dordrecht
Malin D. F., Quinn P. J., Graham J. A., 1983, ApJ, 272, L5
Martin C., The GALEX Team 2005, in Colless M., Staveley-Smith L., Stathakis R. A., eds, Proc. IAU Symp. 216, Maps of the Cosmos. Astron. Soc. Pac., San Francisco, p. 221
Morganti R., 2010, Publ. Astron. Soc. Aust., 27, 463
Morganti R., Robinson A., Fosbury R. A. E., di Serego Alighieri S., Tadhunter C. N., Malin D. F., 1991, MNRAS, 249, 91
Morganti R., Fosbury R. A. E., Hook R. N., Robinson A., Tsvetanov Z., 1992, MNRAS, 256, 1P
Morganti R., Killeen N. E. B., Ekers R. D., Oosterloo T. A., 1999, MNRAS, 307, 750

Morrissey P., et al., 2007, ApJS, 173, 682
Mould J. R. et al., 2000, ApJ, 536, 266
Oosterloo T. A., Morganti R., 2005, A&A, 429, 469
Otsuka M. et al., 2010, A&A, 518, L139
Ott S., 2010, in Mizumoto Y., Morita K.-I., Ohishi M., eds, ASP Conf. Ser. Vol. 434, Astronomical Data Analysis Software and Systems XIX. Astron. Soc. Pac., San Francisco, p. 139
Panuzzo P. et al., 2010, A&A, 518, L37
Parkin et al. 2011, submitted
Peng E. W., Ford H. C., Freeman K. C., White R. L., 2002, AJ, 124, 3144
Peterson B. A., Dickens R. J., Cannon R. D., 1975, Publ. Astron. Soc. Aust., 2, 366
Prescott M. K. M. et al., 2007, ApJ, 668, 182
Rees M. J., 1989, MNRAS, 239, 1P
Rejkuba M., Minniti D., Courbin F., Silva D. R., 2002, ApJ, 564, 688
Relaño M., Lisenfeld U., Pérez-González P. G., Vílchez J. M., Battaner E., 2007, ApJ, 667, L141
Rho J. et al., 2008, ApJ, 673, 271
Roussel H. et al., 2010, A&A, 518, L66
Schiminovich D., van Gorkom J. H., van der Hulst J. M., Kasow S., 1994, ApJ, 423, L101
Silk J., Rees M. J., 1998, A&A, 331, L1
Smith M. W. L. et al., 2010, A&A, 518, L51
Sodroski T. J. et al., 1994, ApJ, 428, 638
Soria R. et al., 1996, ApJ, 465, 79
Stansberry J. A. et al., 2007, PASP, 119, 1038
Stickel M. et al., 2000, in Lemke D., Stickel M., Wilke K., eds, Lecture Notes Phys. Vol. 548, *ISO* Survey of a Dusty Universe. Springer-Verlag, Berlin, p. 251
Stickel M., van der Hulst J. M., van Gorkom J. H., Schiminovich D., Carilli C. L., 2004, A&A, 415, 95
Struve C., Oosterloo T. A., Morganti R., Saripalli L., 2010, A&A, 515, A67
Sutherland R. S., Bicknell G. V., Dopita M. A., 1993, ApJ, 414, 510
Temi P., Mathews W. G., Brighenti F., Bregman J. D., 2003, in Gry C., Peschke S., Matagne J., Garcia-Lario P., Lorente R., Salama A., eds, ESA SP-511, Exploiting the *ISO* Data Archive. Infrared Astronomy in the Internet Age. ESA, Noordwijk, p. 293
Tielens A. G. G. M., 1998, ApJ, 499, 267
Turner T. J., George I. M., Mushotzky R. F., Nandra K., 1997, ApJ, 475, 118
van Breugel W., Fragile C., Anninos P., Murray S., 2004, in Duc P.-A., Braine J., Brinks E., eds, Proc. IAU Symp. 217, Recycling Intergalactic and Interstellar Matter. Astron. Soc. Pac., San Francisco, p. 472
Whittet D. C. B., 2003, Dust in the Galactic Environment. IOP Publishing, Bristol
Wyder T. K. et al., 2007, ApJS, 173, 293
Zhu Y.-N., Wu H., Cao C., Li H.-N., 2008, ApJ, 686, 155

This paper has been typeset from a TEX/LATEX file prepared by the author.